

RESEARCH ARTICLE

MATERIALS SCIENCE

Identification of the Activity Source of CO₂ Electroreduction by Strategic Catalytic Site Distribution in Stable Supramolecular Structure System

Sheng-Nan Sun,^{1,†} Ning Li,^{2,†} Jiang Liu,*¹ Wen-Xin Ji,³ Long-Zhang Dong,¹ Yi-Rong Wang,¹ and Ya-Qian Lan*¹

¹ *Jiangsu Collaborative Innovation Centre of Biomedical Functional Materials, Jiangsu Key Laboratory of New Power Batteries, School of Chemistry and Materials Science, Nanjing Normal University, Nanjing, 210023, P. R. China.*

² *School of Chemistry and Chemical Engineering, Yangzhou University, Yangzhou 225002, P. R. China.*

³ *State Key Laboratory of High-efficiency Coal Utilization and Green Chemical Engineering, Ningxia University, Yinchuan 750021, P. R. China.*

[†] *These authors contributed equally*

*Corresponding authors J. L. (email: liuj@njnu.edu.cn) and Y.-Q. L. (email: yqlan@njnu.edu.cn)

Abstract

Identification of the real catalytic site in CO₂ reduction reaction (CO₂RR) is critical for the rational design of catalyst and the understanding of reactive mechanism. In this study, the catalytic activity of pyridine-containing materials was for the first time structurally demonstrated in CO₂RR by crystalline supramolecular coordination compounds model system. The system consists of three stable supramolecular coordination compounds (Ni-TPYP, Ni-TPYP-1 and Ni-TPP) with different numbers (4, 2 and 0) of active pyridine groups (i.e. uncoordinated pyridine nitrogen atoms). The electrocatalytic test results show that with the decrease of the number of active pyridine groups, the CO₂RR performance is gradually reduced, mainly showing the

reduction of highest FE_{CO} (99.8%, 83.7% and 25.6%, respectively). The crystallographic, experimental and theoretical evidences prove that the CO_2RR activity is more likely derived from uncoordinated pyridine nitrogen than the electrocatalytic inert metal nickel in porphyrin center. This work serves as an important case study for the identification of electrocatalytic activity of pyridine-containing materials in CO_2RR by simple supramolecular model system.

Keywords: strategic catalytic site distribution; supramolecular structure system; active source; CO_2 electroreduction

Introduction

The increasing anthropogenic CO_2 emission associated with fossil fuel consumption is the main culprit in global warming [1-2]. CO_2RR achieved by renewable electricity is an elegant means to alleviate abovementioned issue, because it can convert CO_2 into valuable products (such as CO , HCOOH , CH_4 , etc.) for efficient carbon cycling [3-11]. So far, the reported efficient electrocatalysts in CO_2RR primarily focus on nanostructured materials [12-13] based on metal [14-15] (such as Cu [16-21], Co [22-24], Zn [25], Ni [26-30], etc.) or metal-free active sites (such as C [31], N [32-35], B [36-37], etc.). Among them, N-doped or N-heterocyclic nanostructured electrocatalysts have made great progress in product conversion and Faraday efficiency of CO_2RR , but it is still very difficult to determine the active N sites in these electrocatalysts due to the lack of accurate and clear structural information [38]. Moreover, there are many other factors including defects [39-44], impurities and complicated components that can further affect the identification of accurate active site [45]. In this case, crystalline electrocatalysts for CO_2RR are believed to be good candidates for solving these issues, because their well-defined structures are most favorable for the identification of the catalytically active site and the study of reactive mechanism [46-47]. Therefore, constructing rational crystalline model system to verify the activity of N-containing electrocatalysts is very important to the development of CO_2RR .

However, to date, there are very limited crystalline materials that are reported as electrocatalysts for CO₂RR because of their relatively poor structural stability. Metal-porphyrin applied in CO₂RR has many advantages [48]. Among them, the metal in the porphyrin center can serve as catalytically active site for CO₂RR and the rigid macrocyclic metalloporphyrin molecule with conjugated π-electron system is conducive to the migration of electrons [49-50]. More importantly, they have clear molecular structure and structurally adjustable properties, which are favorable for the study of reaction mechanism and reasonable optimization of catalytic performance [51-52]. Given these advantages, we hope to construct a simple and rational porphyrin-based model system that can be used for the identification of the electrocatalytic activity of N-containing nanomaterials in CO₂RR.

Herein, we designed and synthesized three crystalline supramolecular coordination compounds containing different numbers of active pyridine groups (i.e. uncoordinated pyridine nitrogen atoms) to identify the electrocatalytic activity of pyridine-containing materials in CO₂RR by controlling the catalytic sites. They are Ni-TPYP (TPYP = 5, 10, 15, 20-Tetra (3pyridiyl)-21H, 23H-porphine) with four uncoordinated pyridine N atoms, Ni-TPYP-1 with two uncoordinated pyridine N atoms as well as Ni-TPP (TPP = 5,10,15,20-Tetraphenyl-21H,23H-porphine) with four inactive benzene groups, respectively. All of them can serve as crystalline heterogeneous electrocatalysts for CO₂RR. At present, the metalloporphyrins with excellent CO₂RR properties are mainly porphyrins containing Co, Fe and Cu [51, 53-54], but no porphyrins with Ni [47] show excellent performance for CO₂RR. Moreover, electrochemical inert Ni was chosen to reduce the electroactivity contribution of metal ion, because it has been demonstrated that high free energy is required for Ni to form the *COOH intermediate (an important intermediate during the process of CO₂-to-CO conversion in CO₂RR) in the rate-determining step (RDS) [47, 55]. We thus studied the electrocatalytic CO₂RR performance of Ni-TPYP, Ni-TPYP-1 and Ni-TPP. The experimental results show that as the number of uncoordinated pyridine N atoms decreases, the electrochemical activity and selectivity of these compounds exhibit such a tendency: Ni-TPYP > Ni-TPYP-1 > Ni-TPP. The Faraday efficiency for the CO₂-to-CO conversion (FE_{CO}) of Ni-TPYP, Ni-TPYP-1 and Ni-TPP are 99.8%, 83.7%, and 25.6%, respectively. The crystallographic and experimental results clearly evidence that the superior electrocatalytic CO₂RR

performance of Ni-TPYP is mainly attributed to the uncoordinated active pyridine N atoms. Moreover, theoretical calculations also prove that CO₂ reacts more readily with pyridine N than with metal Ni in porphyrin center.

Results and Discussion

Single-crystal X-ray diffraction analysis reveals that Ni-TPYP and Ni-TPP crystallize in the same tetragonal space group *I*-42*d* (Table S2 and Fig. S1 and S2). And their structures as well as stacking patterns are almost identical. As shown in Fig. 1a and 1c, both compound molecule (Ni-TPYP and Ni-TPP) structures include a metal Ni ion and a pyridine/benzene-modified porphyrin ring (TPYP/TPP). The Ni^{II} ion connected with four N atoms from porphyrin ring displays a square-planar coordination environment (Ni-TPP/Ni-TPYP). The pyridine N atoms of Ni-TPYP are naked. Both complexes further form similar 3D supramolecular structures by π-π stacking interaction and hydrogen bonds (Fig. 1b, d and Fig. S3). Furthermore, no solvent molecules crystallize in their lattice. Ni-TPYP-1 crystallizes in monoclinic space group *P*2₁/*c* (Table S2 and Fig. S4). Each Ni^{II} ion trapped in TPYP center coordinates two N atoms of pyridine from another two TPYP ligands to form a 2D layer and the layers are further stacked into supramolecular coordination compounds by π-π interaction. (Fig. 1e, f and Fig. S5). It is noted that each TPYP ligand in Ni-TPYP-1 still has two uncoordinated pyridine N atoms.

The phase purity of as-synthesized Ni-TPYP, Ni-TPYP-1 and Ni-TPP was determined by comparing their powder X-ray diffraction (PXRD) with simulated patterns derived from single crystal X-ray diffraction (Fig. S7-S9). The pH stability was investigated by immersing the samples of Ni-TPYP, Ni-TPYP-1 and Ni-TPP into different pH aqueous solutions and 0.5 M KHCO₃ aqueous solution ranging from 3 to 13. After 24 hours, PXRD patterns before and after soaking show that no significant changes for each tested sample can be observed, confirming the structural integrity of Ni-TPYP, Ni-TPYP-1 and Ni-TPP under these conditions (Fig. S10-S12). The thermal stability was also studied by thermogravimetric analysis (TGA) under O₂ atmosphere and shown in Fig. S14.

CO₂RR test was carried out in aqueous solution of 0.5 M KHCO₃ (pH = 7.2). CO is the main gaseous product detected by gas chromatography (Fig. S15-S18). The ¹H NMR spectra shows that no liquid product is observed (Fig. S19). The FE_{CO} of Ni-TPYP gradually increases in the potential range (-0.50 to -0.90 V vs. RHE), and

exhibits the highest FE_{CO} (99.8%) at -0.90 V. Interestingly, the FE_{CO} can maintain over 90% in a wide range of potential from -0.70 to -1.20 V (Fig. 2b and Fig. S20). Excellent performance promotes us to explore its reaction mechanism of CO_2RR . Above all, given that central metal in porphyrin is known to be catalytically active site for electrochemical CO_2 reduction to CO. Therefore, for comparison, TPYP ligand was replaced by TPP to synthesize another very similar supramolecular structure (Ni-TPP). However, the corresponding electrochemical test results show that the CO_2RR performance of Ni-TPP is much poorer than that of Ni-TPYP. As we can see from the LSV comparison curves (Fig. 2a), the total current density of Ni-TPP is lower than Ni-TPYP. Moreover, the highest FE_{CO} of Ni-TPP is only 25.6% at -0.90 V (Fig. 2c and Fig. S24), while the FE_{CO} of Ni-TPYP can reach up to 99.8% (Fig. 2e). Besides, the j_{CO} of Ni-TPYP is 10.7 mA cm^{-2} at -0.90 V, which is 18 times larger than that of Ni-TPP (0.6 mA cm^{-2}) (Fig. 2d). Tafel slope for Ni-TPYP ($218.2 \text{ mV dec}^{-1}$) is also smaller than that of Ni-TPP ($230.3 \text{ mV dec}^{-1}$), implying the favorable kinetic for the CO formation [56], which is ascribed to the more efficient charge transfer and larger active surface in the catalytic process (Fig. 3a). To support this surmise, the electrochemical active surface areas (ECSA) for catalysts were estimated based on the double layer capacitive (C_{dl}) by cyclic voltammetry at different scan rates. The result shows that the C_{dl} of Ni-TPYP (10.8 mF cm^{-2}) is indeed larger than that of Ni-TPP (3.1 mF cm^{-2}), which means that Ni-TPYP has a higher reaction speed in CO_2RR process and owns more active sites to contact with electrolyte (Fig. 3b and Fig. S25) [57]. Therefore, the CO_2RR activity of Ni-TPYP is more active than Ni-TPP. Additionally, the TOF of Ni-TPYP is calculated to be 167.9 h^{-1} at -0.90 V, and achieves the maximum value (602.7 h^{-1}) at -1.30 V (Fig. S26). By contrast, the TOF of Ni-TPP is only 7.6 h^{-1} at -0.90 V. In addition, electrochemical impedance spectroscopy (EIS) measurement was carried out to probe the electrocatalytic kinetics on the electrode/electrolyte surface. Fig. 3c demonstrates that Ni-TPYP has much smaller charge transfer resistance than Ni-TPP during the CO_2RR process, indicating Ni-TPYP can transfer electrons from catalysts to reactants more quickly, eventually resulting in largely enhanced activity and selectivity. All these results indicate that Ni-TPYP has a better CO_2RR performance than that of Ni-TPP, indicating that the activity of Ni is poor as a catalytic site. Given the relatively inert electrochemical activity of metal Ni, we infer that there must be other main factors (such as ligand effect) besides Ni for the excellent electroreduction activity of Ni-TPYP.

To gain further insight into the origin of activity of Ni-TPYP, we tested the CO₂RR properties of pure ligands (TPYP and TPP). It clearly shows that the free TPYP ligand demonstrates poor catalytic performance with a maximum value of FE_{CO} only up to 10.1 %. Hydrogen (H₂) is the main products (Fig. S27). Besides, its total current density and j_{co} are all much smaller than that of Ni-TPYP (Fig. 2a-d and 3a). The CO₂RR activities of free TPP ligand is also poorer than that of Ni-TPP, as demonstrated by its current density and FE_{CO} (Fig. S28 and Fig. S31). These results highlight the important role of metal Ni coordination. Once the metal ion Ni was trapped into the porphyrin center (Ni-TPYP), the electrocatalytic performance undergone tremendous changes. Thus, the metal coordination effect should be an indispensable factor responsible for the enhanced electroactivity of Ni-TPYP. Moreover, we found that the total current density of Ni-TPYP is larger than free TPYP (Fig. 2a). So, we inferred that in addition to acting as an active site, the Ni coordination is more likely to enhance the conductivity of supramolecular structure, which is the main reason for the improved electrocatalytic performance of Ni-TPYP. EIS measurement further validates this fact, because Ni-TPYP has much smaller charge transfer resistance than TPYP (Fig. 3c and Fig. S32), which also exists between Ni-TPP and TPP (Fig. S33).

But beyond that, in the case of pure ligand (TPYP/TPP), the FE_{CO} of TPYP (10.1%) is higher than that of TPP (2.6%), which inspires us to speculate that the increase in electroreduction activity for pure ligands is attributed to the modification of active pyridine groups on porphyrin. Moreover, the positive role of active pyridine N in the CO₂RR process has recently been demonstrated in some homogeneous catalysis [58] and nanostructured electrocatalysts (involving N-doped and N-heterocyclic nanomaterials) [31-35], in which pyridine N is considered as the superior catalytically active site and contributes to stabilization of the key intermediate to improve the performance of CO₂RR. These results well coincide with our experimental results. However, they still lack sufficiently clear structure information. According to the above crystallographic and experimental results, our crystalline supramolecular coordination compounds can structurally prove that active pyridine N is indeed an important catalytic site for CO₂RR.

According to the previous studies, in which pyridine was directly used as homogeneous catalyst for carbon dioxide reduction, methanol is the main product

[58-60]. The electrolyte after electrolysis was further detected by headspace injection on gas chromatography. The test result is consistent with the ^1H NMR test result mentioned above, i.e. there is no liquid product such as methanol (Fig. S34). By contrast, we also tested the CO₂RR performance of pyridine under our experimental conditions. The test results are as shown in the Fig. S35, there is no peak corresponding to methanol, which indicating that under our test conditions, pyridine will not reduce CO₂ to methanol when used for CO₂RR. The reason for this phenomenon should be related to the working electrode material. As previously reported, the reduction of pyridine does not occur at all electrode surfaces, because there is a critical surface interaction between pyridine and the working electrode related to pyridine reduction [61].

To further support our speculation that active pyridine N is more suitable catalytic site, supramolecular coordination compounds Ni-TPYP-1 was designed and synthesized, in which the Ni sites are saturated with six N atoms from TPYP ligands and two pyridine N atoms are naked. Thus, the attraction for CO₂ from the metals in porphyrin centers is blocked by their saturated coordination sphere. As a result, CO₂ can be only adsorbed by two naked pyridine N. The highest FE_{CO} of Ni-TPYP-1 can reach up to 83.7% at -0.90 V (Fig. 2b, 2c and Fig. S36) and the j_{CO} of Ni-TPYP-1 is 7.4 mA cm⁻² at -0.90 V vs. RHE (Fig. 2d). Tafel slope for Ni-TPYP-1 is 228.3mV dec⁻¹ (Fig. 3a). And the C_{dl} of Ni-TPYP-1 is 5.4 mF cm⁻² (Fig. 3b). All data indicate that Ni-TPYP-1 with two naked pyridine groups has poorer CO₂RR performance than Ni-TPYP with four naked pyridine groups but much better than Ni-TPP without pyridine groups, which further confirms that active pyridine N is better catalytic site.

In addition, another two isostructural complexes, Co-TPYP-1 and Zn-TPYP-1, which have the same host structure as Ni-TPYP-1, were further synthesized to confirm the accuracy of above conclusions [62-63]. All the metal centers in the porphyrin units of Co-TPYP-1 and Zn-TPYP-1 are saturated with six N atoms, resulting in only two of the four available pyridyl arms of each porphyrin are naked (Fig. S37-S40). The CO₂RR test results show that the electroreduction performance of Co-TPYP-1 is also favorable. At relatively low potential (-0.50 V), its FE_{CO} is 63.0%, and then reaches up to the highest FE_{CO} (93.7%) at -0.70V, which is a little better than Ni-TPYP-1 (Fig. S41). By contrast, the CO₂RR performance of Zn-TPYP-1 is unsatisfactory. The highest FE_{CO} of Zn-TPYP-1 appears at -1.0V with a value of

17.4% (Fig. S42). The difference in CO₂RR performance is related to the type of metal trapped in porphyrin pocket. Different metal coordination effects endow metalloporphyrin complexes with different conductivity, and thus the differences in CO₂RR performance. The results of EIS tests are consistent with our speculation, in which the metalporphyrin conductivity plays an important role in our system and there is such a sequence: Co-TPYP-1 > Ni-TPYP-1 > Zn-TPYP-1 (Fig. S43).

The excellent electrocatalytic performance of Ni-TPYP for CO formation encourages us to evaluate its durability. A 2 hours electrolysis performed with chronoamperometric test was carried out at -0.90 V in CO₂-saturated KHCO₃ aqueous solution. As time goes on, FE_{CO} continues to decline within two hours and the activity remained above 80% in the previous hour (Fig. S44). The reaction liquids were collected and characterized by inductively coupled plasma mass spectrometry (ICP-MS) measurements and UV-visible spectrophotometer (Table S1 and Fig. S45). The content of metal element (Ni) in electrolyte after reaction is lower than the detection limit and there is no characteristic absorption peak of porphyrin in the ultraviolet-visible spectra, proving that no detectable impurities exist in the reaction electrolyte. In addition, the PXRD peaks of the samples before and after the electrochemical test were almost identical (Fig. S46-S48). All these results further confirm the structural stability of electrocatalysts.

To verify the carbon source of the produced carbon monoxide, the isotopic ¹³CO₂ experiment was performed under identical electrocatalytic reaction, and the product was identified by the mass spectrum of ¹³C. As shown in Fig. 3d, the mass spectrogram clearly gives the ¹³C signal, which is in line with previous work [47]. These results unambiguously demonstrate that Ni-TPYP is indeed active for converting CO₂ to CO under electrolytic condition.

Considering a fact that for most catalytic reactions (including CO₂RR), the catalytic activity of heterogeneous catalysts mainly originates from surface / interface catalysis, which may affect the drawing of meaningful structure-property relationships. Because in some cases, the structure of the surface may be different from the bulk crystal structure. Thus, we prepared Ni-TPYP microcrystal powder (as shown in the Fig. S50 and Fig. S51, the size is ~ 2 μm that is similar to the bulk crystal after grounding) through improved synthesis methods. The well-matched PXRD patterns for bulk crystals and microcrystal powder proves the purity of the synthesized

microcrystal powder. Then, we used unground microcrystal powder of Ni-TPYP to prepare electrode and tested its electrocatalytic CO₂RR performance. We found that under the identical electrocatalytic conditions, the main product of unground Ni-TPYP microcrystals is still CO, and FE_{CO} can still reach up to 98.41% (Fig. S52), further demonstrating the reliability of our experimental results and conclusions.

According to the above experimental results, by controlling the catalytically active sites, the CO₂RR activity of pyridine N can be clearly confirmed, as shown in Fig. 4a. When a central four-coordination metal (Ni) and four pyridine groups were naked, the supramolecular compound Ni-TPYP has the highest FE_{CO} (99.8%). While when four pyridine groups are replaced by benzenes (Ni-TPP), the catalytic site at this time is only the metal Ni. The electrochemical test results show that the activity of Ni-TPP is poor, and the maximum value of FE_{CO} is only 25.6%, indicating that Ni is not the best active site. The fact that the CO₂RR performance of TPYP is better than that of TPP inspired us to speculate that the excellent properties of Ni-TPYP maybe mainly due to the pyridine groups modified on porphyrin. Furthermore, the compounds Ni-TPYP-1 with blocked metal Ni (saturated six-coordination) and two naked pyridine groups was synthesized to further demonstrate, in which only two pyridine N can act as catalytic sites. The test results show that the CO₂RR performance of Ni-TPYP-1 is poorer than that of Ni-TPYP but much better than that of Ni-TPP, which further proves the above speculation that active pyridine N is the more suitable catalytic site. However, it is noteworthy that the role of metal Ni can not be ignored, which is more likely to enhance the conductivity of molecular structure by coordination effect in addition to acting as a catalytic site.

Density functional theory (DFT) calculation was carried out to further identify the catalytically active sites in these crystalline electrocatalysts. Generally, four elementary reactions were considered during the CO₂RR process, including the formation of *CO₂, *COOH, *CO and the finally CO desorption processes. There are two kinds of active sites (metal center and pyridine N) were taken into account in our calculations. From the DFT calculation diagrams shown in Fig. 4a and 4b, the RDS for CO₂ reduction is the formation of *COOH. In the case of metal active site, the active Ni in Ni-TPYP (denoted as Ni1) requires free energy of 1.60 eV to form intermediate *COOH, which is almost the same as that of active Ni in Ni-TPP (denoted as Ni2, 1.59 eV). This result indicates that the activity of Ni1 and Ni2 is

similar, and the high energy barriers of *COOH formation show that Ni2 possesses poor activity, so does Ni1. Interestingly, for active pyridine N site in Ni-TPYP (denoted as N), it consumes the lowest energy difference of 0.97 eV to form *COOH. The reduction processes from CO₂ to CO on Ni-TPYP are summarized in Fig. 4c. All in all, the sequence of the reaction energies on different these two active sites reveal that the high CO₂ electroreduction performance for Ni-TPYP is mainly attributed to the active pyridine N.

Conclusion

In summary, by hierarchical controlling the number of catalytic sites in supramolecular coordination compounds crystal model system, the catalytic activity of pyridine-containing materials was for the first time structurally identified in CO₂RR. The system includes Ni-TPYP, Ni-TPYP-1 and Ni-TPP, which have four uncoordinated pyridine N, two uncoordinated pyridine N and none pyridine N atoms, respectively. As the number of uncoordinated pyridine N atoms decreases, the selectivity of the compounds exhibit such a tendency: Ni-TPYP (FE_{CO} = 99.8%) > Ni-TPYP-1 (83.7%) > Ni-TPP (25.6%). These results clearly demonstrated that the electrocatalytic performance for Ni-TPYP mainly comes from the active pyridine N atom. Among them, Ni coordination effect plays a very important role in improving the conductivity of electrocatalyst. Theoretical calculations also show that CO₂ reacts more readily with pyridine N than metal Ni. Significantly, such crystalline supramolecular coordination compounds crystal model system exactly identifies the activity of pyridine N in CO₂RR process. This work provides a simple and accurate supramolecular coordination compounds model system to understand the electrocatalytic activity and reaction mechanism of N-doped and N-heterocyclic nanostructured electrocatalysts in CO₂RR.

Methods

Materials and synthetic procedures: Porphyrin ligands and methanol were obtained from commercial sources. Nickel acetate tetrahydrate (Ni(OAc)₂·4H₂O), Cobalt acetate tetrahydrate (Co(OAc)₂·4H₂O), Zinc nitrate hexahydrate (Zn(NO₃)₂ 6H₂O),

Potassium bicarbonate (KHCO_3), Pyridine (99+ %), Hydrochloric acid (HCl) and N, N-Dimethylformamide (DMF) were supplied by the Shanghai Reagent Factory. Nafion solution (5 wt %) was purchased from Sigma–Aldrich. Carbon paper (CP, TGP-H-060) was bought from Fuel Cell Store. All of the chemicals used in this experiment were analytical grade and used without further purification. All aqueous solutions were prepared with Millipore water ($18.20 \text{ M}\Omega\cdot\text{cm}$). The purity of the gases used are all 99.999 %.

Synthesis of all samples

Synthesis of Ni-TPYP crystal: 6mL mixed solution of deionized water and DMF containing 5, 10, 15, 20-Tetra (3pyridiyl)-21H, 23H-porphine (0.06 g, 0.10 mmol, TPYP), and $\text{Ni}(\text{OAc})_2\cdot 4\text{H}_2\text{O}$ (0.06 g, 0.10 mmol) was placed into a 10 mL scintillation vial and heated at 150°C for 3 days. After cooling down to room temperature with a rate of 10°C h^{-1} , the black octahedral crystal was collected and washed with DMF for several times.

Synthesis of Ni-TPYP-1 crystal: 6mL mixed solution of deionized water, trimethylamine and DMF (2:1:3) containing TPYP (0.03 g, 0.05 mmol), and $\text{Ni}(\text{OAc})_2\cdot 4\text{H}_2\text{O}$ (0.03 g, 0.125 mmol) was placed into a 10 mL scintillation vial and heated at 180°C for 3 days. After cooling down to room temperature with a rate of 10°C h^{-1} , the black diamond crystal was collected and washed with DMF for several times.

Synthesis of Ni-TPP crystal: 5,10,15,20-Tetraphenyl-21H,23H-porphine (0.06 g, 0.10 mmol, TPP) was added to the mixed solution (6 mL) of DMF and deionized water. Then triethylamine (28 μL , 0.20 mmol) was added to the above solution. After sonicated for 30 min., $\text{Ni}(\text{OAc})_2\cdot 4\text{H}_2\text{O}$ (0.06 g, 0.10 mmol) was added into the mixed solution, and sonicated for another 30 min. The solution was placed in a 10 mL scintillation vial and heated at 150°C for 72 hours, and the black octahedral crystal was obtained.

Synthesis of Co-TPYP-1 crystal: The mixed solution of 4mL DMF and 41.61 μL

HCl containing TPYP (0.0062 g, 0.01 mmol) and Co(OAc)₂·4H₂O (0.005 g, 0.02 mmol) was placed into a 10 mL scintillation vial and heated at 150 °C for 2 days. After cooling down to room temperature with a rate of 10 °C h⁻¹, the black diamond crystal was collected and washed with DMF for several times.

Synthesis of Zn-TPYP-1 crystal: 4mL DMF containing TPYP (6.2 mg, 0.01 mmol), and Zn(NO₃)₂ 6H₂O (6.0 mg, 0.02 mmol) was placed into a small capped vial. The vial contents were mixed by sonication and heated at 100 °C for 25 h. After cooling down to room temperature over 35 h, the purple diamond crystal was collected and washed with DMF for several times.

Synthesis of Ni-TPYP microcrystal powder: 0.06 g (0.10 mmol) 5, 10, 15, 20-Tetra (3pyridiyl)-21H, 23H-porphine (TPYP) and 0.06 g (0.10 mmol) Ni(OAc)₂·4H₂O were placed into a 50 mL flask. Then 25mL DMF was added into the flask. The mixture was refluxed for 10 hours. When the reaction is completed, adding a lot of water to precipitate the product. Reddish brown powder (Ni-TPYP microcrystal powder) was collected and washed with H₂O for several times.

Electrochemical measurements

All electrochemical tests of the catalysts were performed on an electrochemical workstation (Bio-Logic) with a standard three-electrode system at room temperature and under ambient conditions. An airtight H-type cell separated by a cation exchange membrane (Nafion®117, dupont) was used as a reactor. Each compartment contained 25 mL electrolyte (0.5 M KHCO₃) with approximately 25 mL headspace. Ag/AgCl electrode (with saturated KCl) and carbon rod were used as the reference electrode and the counter, respectively. The working electrode was a catalyst-modified carbon paper (1 cm × 2 cm, denoted as CPE) in 0.5 M KHCO₃ solution (pH = 7.2).

The polarization curves results were obtained by performing linear sweep voltammetry (LSV) mode with a scan rate of 5 mV s⁻¹ during the CO₂ reduction experiments. Initially, LSV for the modified electrode were recorded in Ar-saturated 0.5 M KHCO₃ (pH=8.8). LSV result in Ar-saturated 0.5 M KHCO₃ was got after

bubbling with CO₂ (99.999%) for at least 30 min to make sure the aqueous solution was saturated. All the LSV curves were presented without IR compensation. After that, the controlled potential electrolysis was conducted. All potentials were measured against an Ag/AgCl reference electrode and the results were converted to those against an reversible hydrogen electrode (RHE) based on the Nernst equation: E (vs. RHE) = E (vs. Ag/AgCl) + 0.1989 V + 0.059 × pH.

Electrochemical active surface area (ECSA) measurement was estimated by performing cyclic voltammograms (CV) at different scan rates from 10 to 100 mV s⁻¹ under the potential window of -0.18 V to -0.06 V (vs. RHE) to measure the double-layer capacitance (C_{dl}).

Electrochemical impedance spectroscopy (EIS) measurement was carried out on the electrochemical analyzer in a frequency range from 1000 kHz to 100 mHz at an overpotential of -0.90 V vs. RHE.

Supplementary data

Supplementary data are available at NSR online.

Acknowledgements

This work was financially supported by NSFC (No. 21622104, 21701085, 21871141 21871142 and 21901122); the NSF of Jiangsu Province of China (No. BK20171032); the Natural Science Research of Jiangsu Higher Education Institutions of China (No. 17KJB150025 and 19KJB150011) and Project funded by China Postdoctoral Science Foundation (No. 2018M630572 and 2019M651873); Priority Academic Program Development of Jiangsu Higher Education Institutions and the Foundation of Jiangsu Collaborative Innovation Center of Biomedical Functional Materials; The East-West Cooperation Project of Ningxia Key R & D Plan (No. 2019BFH02014).

Received: ((will be filled in by the editorial staff))

Revised: ((will be filled in by the editorial staff))

Published online: ((will be filled in by the editorial staff))

Conflict of interest statement

None declared.

Author contributions

Y.-Q. L. and J. L. conceived the idea. S.-N. S. and N. L. designed the experiments, collected and analyzed the data. W.-X. J. accomplished the theoretical calculation. L.-Z. D. and Y.-R. W. assisted with the experiments and characterizations. S.-N. S. wrote the manuscript. All authors discussed the results and commented on the manuscript.

References

1. Shakun J D, Clark P U, He F *et al.* Global warming preceded by increasing carbon dioxide concentrations during the last deglaciation. *Nature* 2012; **484**: 49.
2. Zhu D D and Liu J LQiao S Z. Recent advances in inorganic heterogeneous electrocatalysts for reduction of carbon dioxide. *Adv. Mater.* 2016; **28**: 3423-3452.
3. Gao D, Arán-Ais R M, Jeon H S *et al.* Rational catalyst and electrolyte design for CO₂ electroreduction towards multicarbon products. *Nat. Catal.* 2019; **2**: 198-210.
4. Wang H, Liang Z, Tang M *et al.* Self-selective catalyst synthesis for CO₂ reduction. *Joule* 2019; **3**: 1927-1936
5. Varela A S and Ju WStrasser P. Molecular nitrogen–carbon catalysts, solid metal organic framework catalysts, and solid metal/nitrogen-doped carbon (MNC) catalysts for the electrochemical CO₂ reduction. *Adv. Energy Mater.* 2018; **8**: 1703614.
6. Vasileff A and Zheng YQiao S Z. Carbon solving carbon's problems: recent progress of nanostructured carbon-based catalysts for the electrochemical reduction of CO₂. *Adv. Energy Mater.* 2017; **7**: 1700759.
7. Zhi X, Jiao Y, Zheng Y *et al.* Impact of interfacial electron transfer on electrochemical CO₂ reduction on graphitic carbon nitride/doped graphene. *Small* 2019; **15**: 1804224.

8. Li Q, Fu J, Zhu W *et al.* Tuning Sn-catalysis for electrochemical reduction of CO₂ to CO via the core/shell Cu/SnO₂ structure. *J. Am. Chem. Soc.* 2017; **139**: 4290-4293.
9. Wang Y, Chen Z, Han P *et al.* Single-atomic Cu with multiple oxygen vacancies on ceria for electrocatalytic CO₂ reduction to CH₄. *ACS Catal.* 2018; **8**: 7113-7119.
10. Elouarzaki K, Kannan V, Jose V *et al.* Recent trends, benchmarking, and challenges of electrochemical reduction of CO₂ by molecular catalysts. *Adv. Energy Mater.* 2019; **9**: 1900090.
11. Wang Y, Chen J, Wang G *et al.* Perfluorinated covalent triazine framework derived hybrids for the highly selective electroconversion of carbon dioxide into methane. *Angew. Che. Int. Ed.* 2018; **57**: 13120-13124.
12. Liu J, Guo C, Vasileff A *et al.* Nanostructured 2D materials: prospective catalysts for electrochemical CO₂ reduction. *Small Methods* 2017; **1**: 1600006.
13. De Luna P, Quintero-Bermudez R, Dinh C-T *et al.* Catalyst electro-redistribution controls morphology and oxidation state for selective carbon dioxide reduction. *Nat. Catal.* 2018; **1**: 103-110.
14. Wang Y, Liu J, Wang Y *et al.* Tuning of CO₂ reduction selectivity on metal electrocatalysts. *Small* 2017; **13**: 1701809.
15. Chen Y, Ji S, Chen C *et al.* Single-atom catalysts: synthetic strategies and electrochemical applications. *Joule* 2018; **2**: 1242-1264.
16. Dinh C-T, Burdyny T, Kibria M G *et al.* CO₂ electroreduction to ethylene via hydroxide-mediated copper catalysis at an abrupt interface. *Science* 2018; **360**: 783-787.
17. Shinagawa T, Larrazábal G O, Martín A J *et al.* Sulfur-modified copper catalysts for the electrochemical reduction of carbon dioxide to formate. *ACS Catal.* 2018; **8**: 837-844.
18. Ma M and Djanashvili KSmith W A. Controllable hydrocarbon formation from the electrochemical reduction of CO₂ over Cu nanowire arrays. *Angew. Chem. Int. Ed.* 2016; **55**: 6680-6684.

19. Jiao Y, Zheng Y, Chen P *et al.* Molecular scaffolding strategy with synergistic active centers to facilitate electrocatalytic CO₂ reduction to hydrocarbon/alcohol. *J. Am. Chem. Soc.* 2017; **139**: 18093-18100.
20. Gu Z, Shen H, Shang L *et al.* Nanostructured copper-based electrocatalysts for CO₂ reduction. *Small Methods* 2018; **2**: 1800121.
21. Peng M, Ci S, Shao P *et al.* Cu₃P/C nanocomposites for efficient electrocatalytic CO₂ reduction and Zn-CO₂ battery. *J. Nanosci. and Nanotechno.* 2019; **19**: 3232-3236.
22. Wang X, Chen Z, Zhao X *et al.* Regulation of coordination number over single Co sites: triggering the efficient electroreduction of CO₂. *Angew. Chem. Int. Ed.* 2018; **57**: 1944-1948.
23. Gao S, Lin Y, Jiao X *et al.* Partially oxidized atomic cobalt layers for carbon dioxide electroreduction to liquid fuel. *Nature* 2016; **529**: 68.
24. Pan Y, Lin R, Chen Y *et al.* Design of single-atom Co-N₅ catalytic site: a robust electrocatalyst for CO₂ reduction with nearly 100% CO selectivity and remarkable stability. *J. Am. Chem. Soc.* 2018; **140**: 4218-4221.
25. Jeon H S, Sinev I, Scholten F *et al.* Operando evolution of the structure and oxidation state of size-controlled Zn nanoparticles during CO₂ electroreduction. *J. Am. Chem. Soc.* 2018; **140**: 9383-9386.
26. Yang H B, Hung S-F, Liu S *et al.* Atomically dispersed Ni(i) as the active site for electrochemical CO₂ reduction. *Nat. Energy* 2018; **3**: 140-147.
27. Zheng T, Jiang K, Ta N *et al.* Large-scale and highly selective CO₂ electrocatalytic reduction on nickel single-atom catalyst. *Joule* 2019; **3**: 265-278.
28. Li X, Bi W, Chen M *et al.* Exclusive Ni-N₄ sites realize near-unity CO selectivity for electrochemical CO₂ reduction. *J. Am. Chem. Soc.* 2017; **139**: 14889-14892.
29. Zhao C, Dai X, Yao T *et al.* Ionic exchange of metal-organic frameworks to access single nickel sites for efficient electroreduction of CO₂. *J. Am. Chem. Soc.* 2017; **139**: 8078-8081.

30. Gong Y-N, Jiao L, Qian Y *et al.* Regulating the coordination environment of MOF-templated single-atom nickel electrocatalysts for boosting CO₂ reduction. *Angew. Chem. Int. Ed.* 2020; **59**: 2705-2709.
31. Wu J J, Ma S C, Sun J *et al.* A metal-free electrocatalyst for carbon dioxide reduction to multi-carbon hydrocarbons and oxygenates. *Nat. Commun.* 2016; **7**: 6.
32. Sharma P P, Wu J, Yadav R M *et al.* Nitrogen-doped carbon nanotube arrays for high-efficiency electrochemical reduction of CO₂: on the understanding of defects, defect density, and selectivity. *Angew. Chem.* 2015; **127**: 13905-13909.
33. Wu J, Yadav R M, Liu M *et al.* Achieving highly efficient, selective, and stable CO₂ reduction on nitrogen-doped carbon nanotubes. *ACS Nano* 2015; **9**: 5364-5371.
34. Song Y, Chen W, Zhao C *et al.* Metal-free nitrogen-doped mesoporous carbon for electroreduction of CO₂ to ethanol. *Angew. Chem. Int. Ed.* 2017; **56**: 10840-10844.
35. Ye L, Ying Y, Sun D *et al.* Highly efficient porous carbon electrocatalyst with controllable N-species content for selective CO₂ reduction. *Angew. Chem. Int. Ed.* 2020; **59**: 3244-3251.
36. Sreekanth N, Nazrulla M A, Vineesh T V *et al.* Metal-free boron-doped graphene for selective electroreduction of carbon dioxide to formic acid/formate. *Chem. Commun.* 2015; **51**: 16061-16064.
37. Mou S, Wu T, Xie J *et al.* Boron phosphide nanoparticles: a nonmetal catalyst for high-selectivity electrochemical reduction of CO₂ to CH₃OH. *Adv. Mater.* 2019; **0**: 1903499.
38. Huan T N, Ranjbar N, Rousse G *et al.* Electrochemical reduction of CO₂ catalyzed by Fe-N-C materials: a structure-selectivity study. *ACS Catal.* 2017; **7**: 1520-1525.
39. Huang J, Cao Y, Wang H *et al.* Revealing active-site structure of porous nitrogen-defected carbon nitride for highly effective photocatalytic hydrogen evolution. *Chem. Eng. J.* 2019; **373**: 687-699.

40. Wu J, Ma S, Sun J *et al.* A metal-free electrocatalyst for carbon dioxide reduction to multi-carbon hydrocarbons and oxygenates. *Nat. Commun.* 2016; **7**: 13869.
41. Zhang J, Yin R, Shao Q *et al.* Oxygen vacancies in amorphous InO_x nanoribbons enhance CO_2 adsorption and activation for CO_2 electroreduction. *Angew. Chem. Int. Ed.* 2019; **58**: 5609-5613.
42. Wang Q, Lei Y, Wang D *et al.* Defect engineering in earth-abundant electrocatalysts for CO_2 and N_2 reduction. *Energy Environ. Sci.* 2019; **12**: 1730-1750.
43. Gu Z, Yang N, Han P *et al.* Oxygen vacancy tuning toward efficient electrocatalytic CO_2 reduction to C_2H_4 . *Small Methods* 2019; **3**: 1800449.
44. Wang Y, Han P, Lv X *et al.* Defect and interface engineering for aqueous electrocatalytic CO_2 reduction. *Joule* 2018; **2**: 2551-2582.
45. Duan Y-X, Meng F-L, Liu K-H *et al.* Amorphizing of Cu nanoparticles toward highly efficient and robust electrocatalyst for CO_2 reduction to liquid fuels with high faradaic efficiencies. *Adv. Mater.* 2018; **30**: 1706194.
46. Hod I, Sampson M D, Deria P *et al.* Fe-porphyrin-based metal-organic framework films as high-surface concentration, heterogeneous catalysts for electrochemical reduction of CO_2 . *ACS Catal.* 2015; **5**: 6302-6309.
47. Wang Y-R, Huang Q, He C-T *et al.* Oriented electron transmission in polyoxometalate-metallocporphyrin organic framework for highly selective electroreduction of CO_2 . *Nat. Commun.* 2018; **9**: 4466.
48. Huang Q, Li Q, Liu J *et al.* Disclosing CO_2 activation mechanism by hydroxyl-induced crystalline structure transformation in electrocatalytic process. *Matter* 2019; **1**: 1656-1668.
49. Yang X-L, Xie M-H, Zou C *et al.* Porous metallocporphyrinic frameworks constructed from metal 5,10,15,20-Tetrakis(3,5-biscarboxylphenyl)porphyrin for highly efficient and selective catalytic oxidation of alkylbenzenes. *J. Am. Chem. Soc.* 2012; **134**: 10638-10645.

50. Xie M-H and Yang X-LWu C-D. A metalloporphyrin functionalized metal-organic framework for selective oxidization of styrene. *Chem. Commun.* 2011; **47**: 5521-5523.
51. Weng Z, Jiang J, Wu Y *et al.* Electrochemical CO₂ reduction to hydrocarbons on a heterogeneous molecular Cu catalyst in aqueous solution. *J. Am. Chem. Soc.* 2016; **138**: 8076-8079.
52. Gotico P, Boitrel B, Guillot R *et al.* Second-sphere biomimetic multipoint hydrogen-bonding patterns to boost CO₂ reduction of iron porphyrins. *Angew. Chem. Int. Ed.* 2019; **58**: 4504-4509.
53. Hu X-M, Rønne M H, Pedersen S U *et al.* Enhanced catalytic activity of cobalt porphyrin in CO₂ electroreduction upon immobilization on carbon materials. *Angew. Chem. Int. Ed.* 2017; **56**: 6468-6472.
54. Mohamed E A and Zahran Z NNaruta Y. Efficient heterogeneous CO₂ to CO conversion with a phosphonic acid fabricated cofacial iron porphyrin dimer. *Chem. Mater.* 2017; **29**: 7140-7150.
55. Zhang Z, Xiao J, Chen X-J *et al.* Reaction mechanisms of well-defined metal-N₄ sites in electrocatalytic CO₂ reduction. *Angew. Chem. Int. Ed.* 2018; **57**: 16339-16342.
56. Cheng Q, Mao K, Ma L *et al.* Encapsulation of iron nitride by Fe-N-C shell enabling highly efficient electroreduction of CO₂ to CO. *ACS Energy Lett.* 2018; **3**: 1205-1211.
57. Liu S, Xiao J, Lu X F *et al.* Efficient electrochemical reduction of CO₂ to HCOOH over sub-2 nm SnO₂ quantum wires with exposed grain boundaries. *Angew. Chem. Int. Ed.* 2019; **58**: 8499-8503.
58. Yan Y, Zeitler E L, Gu J *et al.* Electrochemistry of aqueous pyridinium: exploration of a key aspect of electrocatalytic reduction of CO₂ to methanol. *J. Am. Chem. Soc.* 2013; **135**: 14020-14023.
59. Keith J A and Carter E A. Theoretical insights into pyridinium-based photoelectrocatalytic reduction of CO₂. *J. Am. Chem. Soc.* 2012; **134**: 7580-7583.

60. Barton E E and Rampulla D MBocarsly A B. Selective solar-driven reduction of CO₂ to methanol using a catalyzed p-GaP based photoelectrochemical Cell. *J. Am. Chem. Soc.* 2008; **130**: 6342-6344.
61. Barton Cole E, Lakkaraju P S, Rampulla D M *et al.* Using a one-electron shuttle for the multielectron reduction of CO₂ to methanol: kinetic, mechanistic, and structural insights. *J. Am. Chem. Soc.* 2010; **132**: 11539-11551.
62. Lipstman S and Goldberg I. Supramolecular crystal chemistry of tetra(3-pyridyl)porphyrin. 2. two- and three-dimensional coordination networks with cobalt and cadmium ions. *Cry. Growth Des.* 2010; **10**: 5001-5006.
63. Choi E-Y, DeVries L D, Novotny R W *et al.* An interdigitated metalloporphyrin framework: two-dimensional tessellation, framework flexibility, and selective guest accommodation. *Cryst. Growth Des.* 2010; **10**: 171-176.

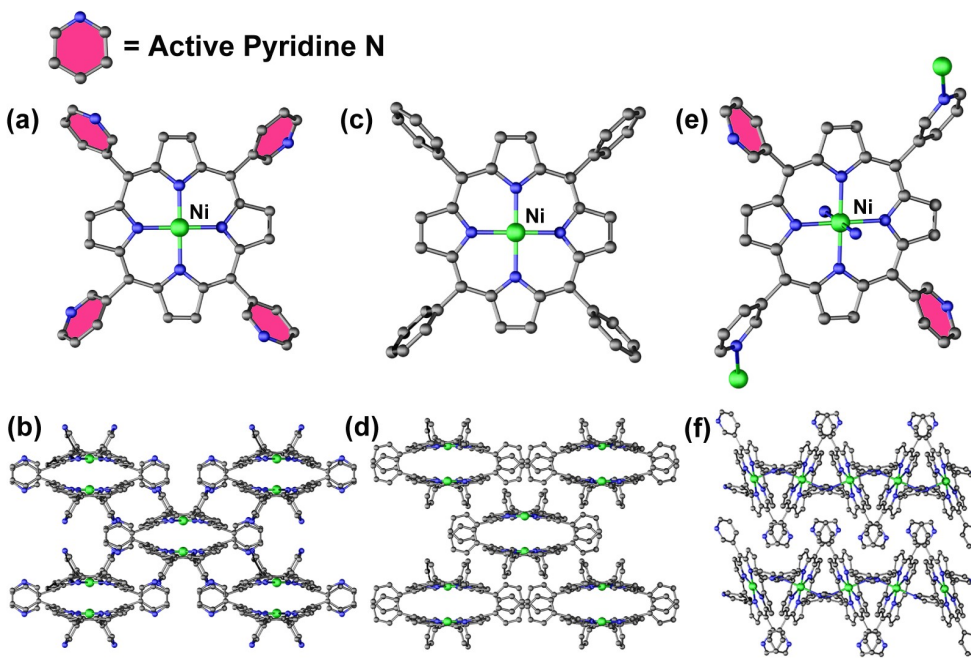


Fig. 1. (a, c, e) The molecular structures of Ni-TPYP, Ni-TPP and Ni-TPYP-1, (b, d, f) The supramolecular stacked structures of Ni-TPYP, Ni-TPP and Ni-TPYP-1. Color code: C, black; N, blue; Ni, green.

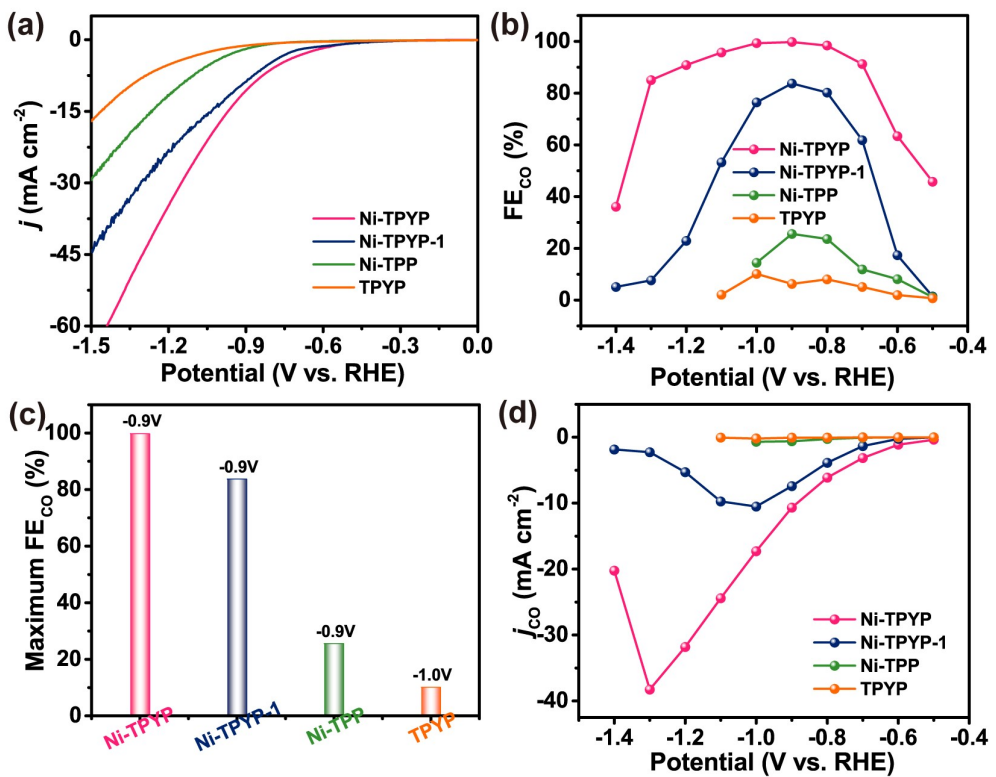


Fig. 2. (a) LSVs of Ni-TPYP, Ni-TPYP-1, Ni-TPP and TPYP in CO_2 -saturated 0.5 M KHCO_3 solution, (b) FE_{CO} of Ni-TPYP, Ni-TPYP-1, Ni-TPP and TPYP in CO_2 -saturated 0.5 M KHCO_3 solution, (c) Maximum FE_{CO} of Ni-TPYP (-0.90 V), Ni-TPYP-1 (-0.90 V), Ni-TPP (-0.90 V), TPYP (-1.00 V), (d) j_{CO} of Ni-TPYP, Ni-TPYP-1, Ni-TPP and TPYP.

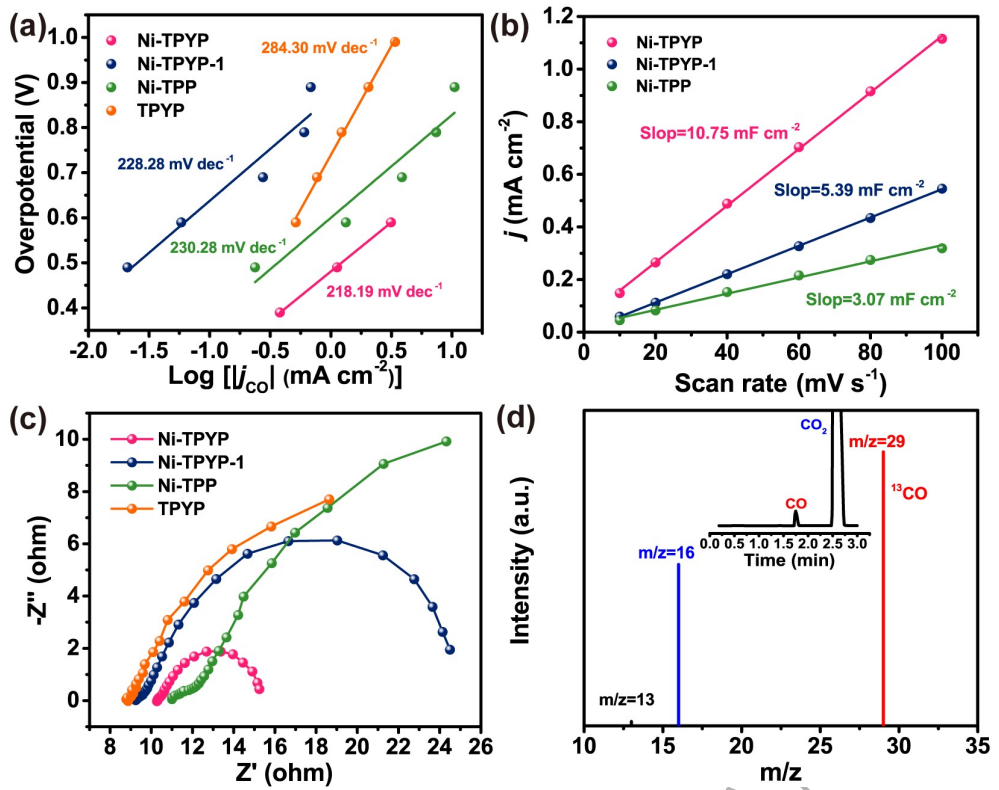


Fig. 3. (a) Tafel plots of Ni-TPYP, Ni-TPYP-1, Ni-TPPP and TPYP, (b) C_{dl} of Ni-TPYP, Ni-TPYP-1 and Ni-TPPP, (c) Nyquist plots of electrocatalysts over the frequency ranging from 1000 kHz to 0.1 Hz at -0.9 V vs. RHE, (d) The mass spectra of ^{13}CO recorded under $^{13}\text{CO}_2$ atmosphere.

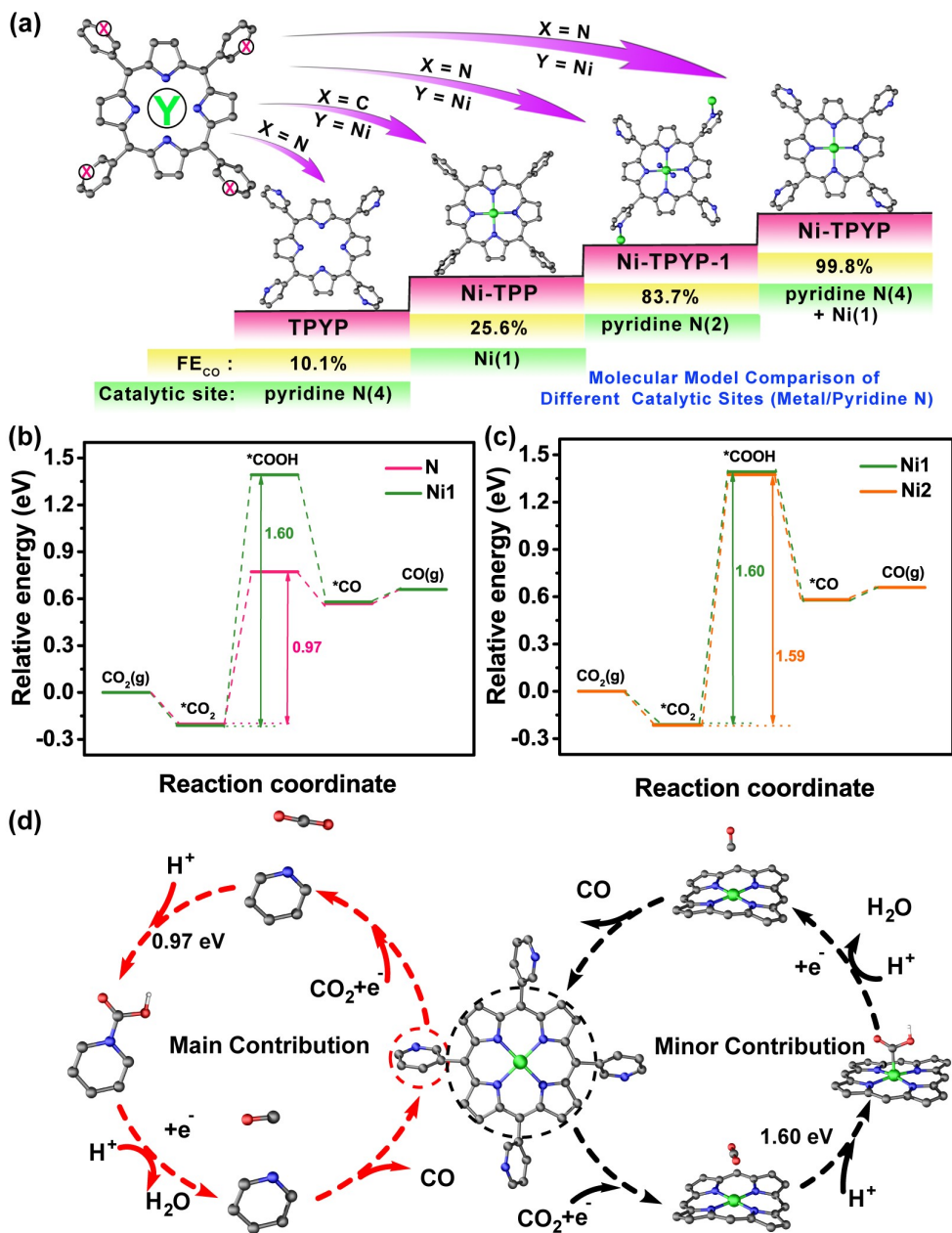


Fig. 4. (a) Comparison of different molecular structures and catalytic sites (Ni-TPYP, Ni-TPYP-1, Ni-TPP and TPYP), (b, c) Calculated free energy profile for CO₂RR toward the production of CO, (d) Simulated CO₂-to-CO conversion reactive pathway over Ni-TPYP molecule.